AIAA Journal
Vol. 36, No. 10, October 1998

Near-Wall k–ε Computation of Transonic Turbomachinery Flows with Tip Clearance

G. A. Gerolymos,* G. Tsanga,† and I. Vallet‡
Université Pierre-et-Marie-Curie, 91405 Orsay, Paris, France

A computational method for the numerical integration of the Favre–Reynolds averaged, three-dimensional compressible Navier–Stokes equations in axial turbomachinery, using the Launder–Sharma near-wall k–ε turbulence closure, is developed. The mean flow and turbulence transport equations are discretized using a finite volume method based on MUSCL Van Leer flux-vector splitting with Van Albada limiters and are integrated in time using a fully coupled, approximately factored, implicit backward Euler method. The resulting scheme is robust and was found stable for local time steps of Courant–Friedrichs–Lewy number (CFL) = 20. The computational domain is discretized using a basic H–O–H grid. The tip-clearance gap is discretized using a fine O-type grid. The radial distribution of nodes within the tip-clearance gap is independent of the blade-row O grid, and a buffer overlap grid is used to convey information. Boundary conditions at periodicity boundaries and at domain interfaces are treated using five phantom nodes. This procedure ensures stability at high CFL. Results are presented for the NASA 37 rotor, at an operating point near surge. Computations are compared with measurements both for blade-to-blade Mach number contours and pitchwise distributions and for radial distributions downstream of the blades. Results are obtained using three grids of 10^6, 2×10^6, and 3×10^6 points, with 21, 31, and 41 radial stations within the tip-clearance gap, respectively, demonstrating that results are grid independent. Comparison with measurements is satisfactory, with the exception of pressure ratio overestimation due to unsatisfactory prediction of flow separation by the turbulence model.

Nomenclature

i, j, k	= three-dimensional grid indices
$k_{\mathrm{O-OZ}}$	= O-grid radial surface corresponding to the beginning of the OZ grid
$\breve{M}_{W_{x\theta,ad}}$	= relative Mach number computed using the x and θ velocity components and rothalpy conservation[47,48]
$\dot{m}$	= mass flow
$\dot{m}_{\mathrm{CH}}$	= maximum mass flow (choke mass flow) at nominal rotor speed
N_i, N_j, N_k	= number of grid points, i-wise, j-wise, k-wise
N_{ijk}	= number of grid points, $N_i N_j N_k$
n_{it}	= iteration number
n_w^+	= nondimensional distance of the first grid point from the wall, $n u_\tau \breve{\nu}_w^{-1}$, where n is the distance from the wall, u_τ the friction velocity, and $\breve{\nu}_w$ the kinematic viscosity at the wall
r_j, r_k	= geometric progression ratio for grid-point stretching, j-wise and k-wise
T_u	= turbulence intensity
x, R, θ	= cylindrical system of coordinates, where x is the engine axis
$\breve{\alpha}_{x\theta}$	= angle between the x and θ components of pitchwise mass-averaged absolute velocity
Δs_{O}	= mass flow averaged entropy increase between O-grid inflow and O-grid outflow
δ_{TC}	= tip-clearance height
$\pi_{\mathrm{T-T}}$	= total-to-total pressure ratio
$\pi_{\mathrm{T-T_O}}$	= total-to-total pressure ratio between O-grid inflow and O-grid outflow
χ	= blade chord
χ_x	= axial blade chord

Subscripts

DH	= downstream H-type grid
in	= inflow
M	= pitchwise averaged quantities (meridional)
O	= O-type grid, O grid around the blades
OZ	= buffer O-type grid between clearance-gap grid (TC) and O
out	= outflow
T	= turbulent
TC	= clearance-gap grid
t	= total
UH	= upstream H grid
W	= relative
w	= wall

Superscripts

$\tilde{}$	= Favre average
$\bar{}$	= Reynolds average (ensemble average)
$\breve{}$	= function of averaged quantities that is neither a Favre average nor a Reynolds average

Received Oct. 15, 1997; revision received April 16, 1998; accepted for publication May 21, 1998.

*Professor and Director, Laboratoire d'Energétique, Unité Associée au Centre National de Recherche Scientifique, Bâtiment 511.

†Graduate Student, Laboratoire d'Energétique, Unité Associée au Centre National de Recherche Scientifique, Bâtiment 511.

‡Assistant Professor, Laboratoire d'Energétique, Unité Associée au Centre National de Recherche Scientifique, Bâtiment 511.

Introduction

THERE is a definite trend toward using transport-equation turbulence closures, such as k–ε, in computational fluid dynamics (CFD).[1,2] They are superior to algebraic closures not only because they give better results, but also because they offer better physical insight and grid independence of results. There exist many three-dimensional Navier–Stokes turbomachinery codes, but very few use transport-equation closures with wall functions,[3–5] and still fewer include near-wall, low-turbulence Reynolds number effects.[6–12] This is due to the difficulty in solving the additional turbulence transport equations.

Hah[6] and Hah et al.[7] use the near-wall, low-turbulence Reynolds number k–ε model of Chien.[13] The equations are solved using an implicit pressure-based scheme, with quadratic upwind discretization of convective terms.[14] The method has been used for the computation of many turbomachinery configurations, both axial and centrifugal.[15–18] The nondimensional distance from the wall of the first grid point nearest to it, $n_w^+ = n u_\tau \breve{\nu}_w^{-1}$, is $n_w^+ \sim 1$–5.

Knight and Choi[8] use the near-wall, low-turbulence Reynolds number $\sqrt{k}-\omega_T$ model of Coakley.[19] The equations are solved using the implicit finite volume upwind scheme developed by Coakley,[20] with Courant–Friedrichs–Lewy number (CFL) = 3–5 and $n_w^+ \sim 1$. The method is applied to the computation of a turbine cascade.

Kunz and Lakshminarayana[9] use the near-wall, low-turbulence Reynolds number k–ε model of Chien.[13] The numerical scheme uses a centered space discretization with explicit Runge–Kutta time integration,[21] with CFL $= 2\sqrt{2}$ and $n_w^+ \sim 1 - \frac{3}{2}$. The method has been applied to the computation of compressible axial turbomachinery flows.[9,22]

Ameri et al.[10] use the near-wall, low-turbulence Reynolds number k–ω_T model of Wilcox.[23] The numerical scheme uses a centered space-discretization with Runge–Kutta time integration, including implicit residual smoothing and multigrid.[11] The method has been applied to the computation of compressible axial turbine flows.[10–12]

Tip-clearance leakage has a major effect on flow structure over a substantial part of the span.[24–26] Several computational methods try to include the global effects of tip leakage without computing the detailed flow within the tip-clearance gap. Several workers[24] use simplified models based on the momentum equation applied locally across the blade. Many CFD codes use the pinched tip approach[27] where, for relatively thin blades, the tip of the blade is artificially cusped to join together the suction-side and pressure-side grids within the gap. This approach models the gross effects of tip-clearance flows, although the tip geometry is not modeled exactly.

To compute the flow within the gap, an embedded grid technique must be used.[15–18,22,28–32] Rai[28,29] used an embedded O grid (within a blade O grid) with five radial stations within the gap. Liu and Bozzola[30] used an embedded H grid (within a blade H grid) with eight radial stations within the gap. Copenhaver et al.,[15,16] Hah et al.,[17] and Hah and Loellbach[18] used an embedded H grid (within a blade H grid) with 6–10 radial stations within the gap. Kunz et al.[22] and Basson and Lakshminarayana[31] used an embedded H grid (within a blade H grid) with 11–21 radial stations within the gap. Ameri et al.[10] and Ameri and Steinthorsson[11,12] used an embedded O grid (within a blade O grid) with 20–40 radial stations within the gap. Chima[32] used an embedded O grid (within a blade C grid) with 13 radial stations within the gap. The radial resolution of all of these computations is coarse within the gap, with the exception of the work of Ameri et al.[10–12]

The purpose of the present work is to extend an efficient and robust three-dimensional compressible Navier–Stokes solver with near-wall multiequation turbulence closures, developed by Vallet[33] and Gerolymos and Vallet,[34,35] to the computation of three-dimensional transonic turbomachinery flows. Particular care was taken to correctly compute the flow within the tip, by using a multiblock grid technique.[36]

Flow Model

The flow is modeled by the compressible Favre–Reynolds averaged, three-dimensional Navier–Stokes equations, with the Launder–Sharma[37] near-wall k–ε closure, written in tensor-invariant form[1,34,38]:

$$\frac{\partial \bar{\rho}}{\partial t} + \operatorname{div}[\bar{\rho}\tilde{\boldsymbol{W}}] = 0$$

$$\frac{\partial \bar{\rho}\tilde{\boldsymbol{W}}}{\partial t} + \operatorname{div}[\bar{\rho}\tilde{\boldsymbol{W}} \otimes \tilde{\boldsymbol{W}} + \bar{p}\boldsymbol{I} - \bar{\boldsymbol{\tau}} + \widetilde{\rho \boldsymbol{W}'' \otimes \boldsymbol{W}''}]$$
$$= -2\bar{\rho}\boldsymbol{\Omega} \times \tilde{\boldsymbol{W}} - \bar{\rho}\operatorname{grad}\left(-\frac{1}{2}\Omega^2 R^2\right)$$

$$\frac{\partial(\bar{\rho}\breve{H}_R - \bar{p})}{\partial t} + \operatorname{div}[\bar{\rho}\tilde{\boldsymbol{W}}\breve{H}_R - \tilde{\boldsymbol{W}} \cdot (\bar{\boldsymbol{\tau}} - \widetilde{\rho \boldsymbol{W}'' \otimes \boldsymbol{W}''})$$
$$+ (\bar{\boldsymbol{q}} + \widetilde{\rho e'' \boldsymbol{W}''})] = -\left(P_k - \bar{\rho}\varepsilon^* - 2\breve{\mu}\left[\operatorname{grad}\sqrt{k}\right]^2\right)$$

$$\frac{\partial \bar{\rho}k}{\partial t} + \operatorname{div}\left[\bar{\rho}\tilde{\boldsymbol{W}}k - \left(\breve{\mu} + \frac{\mu_T}{\sigma_k}\right)\operatorname{grad} k\right]$$
$$= \left(P_k - \bar{\rho}\varepsilon^* - 2\breve{\mu}\left[\operatorname{grad}\sqrt{k}\right]^2\right)$$

$$\frac{\partial \bar{\rho}\varepsilon^*}{\partial t} + \operatorname{div}\left[\bar{\rho}\tilde{\boldsymbol{W}}\varepsilon^* - \left(\breve{\mu} + \frac{\mu_T}{\sigma_\varepsilon}\right)\operatorname{grad}\varepsilon^*\right]$$
$$= \left(C_{\varepsilon 1} P_k \frac{\varepsilon^*}{k} - C_{\varepsilon 2}\left(Re_T^*\right)\bar{\rho}\frac{\varepsilon^{*2}}{k} + 2\frac{\breve{\mu}\mu_T}{\bar{\rho}}[\nabla^2 \tilde{\boldsymbol{W}}]^2\right) \tag{1}$$

$$\bar{p} = \bar{\rho} R_g \tilde{T} = \bar{\rho}[(\gamma - 1)/\gamma]\tilde{h} = \bar{\rho}(\gamma - 1)\tilde{e}$$

$$-\widetilde{\rho \boldsymbol{W}'' \otimes \boldsymbol{W}''} \cong 2\mu_T\left[\breve{\boldsymbol{D}} - \tfrac{1}{3}\operatorname{div}\tilde{\boldsymbol{W}}\boldsymbol{I}\right] - \tfrac{2}{3}\bar{\rho}k\boldsymbol{I}$$

$$\widetilde{\rho e'' \boldsymbol{W}''} \cong -\kappa_T \operatorname{grad}\tilde{T} \tag{2}$$

$$\breve{H}_R = \tilde{h} + \tfrac{1}{2}\tilde{W}^2 - \tfrac{1}{2}\Omega^2 R^2, \qquad \bar{\rho}\varepsilon^* = \bar{\rho}\varepsilon - 2\breve{\mu}\left[\operatorname{grad}\sqrt{k}\right]^2$$

$$P_k = -\widetilde{\rho \boldsymbol{W}'' \otimes \boldsymbol{W}''} : \breve{\boldsymbol{D}}, \qquad \bar{\boldsymbol{\tau}} \cong 2\breve{\mu}\left[\breve{\boldsymbol{D}} - \tfrac{1}{3}\operatorname{div}\tilde{\boldsymbol{W}}\boldsymbol{I}\right]$$

$$\bar{\boldsymbol{q}} \cong -\breve{\kappa}\operatorname{grad}\tilde{T}, \qquad \breve{\boldsymbol{D}} = \tfrac{1}{2}[\operatorname{grad}\tilde{\boldsymbol{W}} + (\operatorname{grad}\tilde{\boldsymbol{W}})^T]$$

where t is the time; $\otimes$ is the tensor product between two vectors; $\tilde{\boldsymbol{W}}$ is the relative velocity; $\bar{\rho}$ is the density; $\bar{p}$ is the pressure; $\tilde{T}$ is the temperature; $\tilde{h}$ is the enthalpy; $\gamma = 1.4$ is the isentropic exponent for air; $R_g = 287.04$ m^2 s^{-2} K^{-1} is the gas constant for air; $\breve{H}_R = \tilde{h} + \frac{1}{2}\tilde{W}^2 - \frac{1}{2}\Omega^2 R^2$ is the rothalpy of the mean flow,[33,35] which is different from Favre-averaged rothalpy $\tilde{H}_R = \breve{H}_R + k$; k is the turbulence-kinetic energy; ε^* is the modified-dissipation rate of the turbulence-kinetic energy; ε is the dissipation rate; P_k is the turbulence-kinetic-enrergy production; $\bar{\boldsymbol{\tau}}$ is the viscous-stress tensor; $\bar{\boldsymbol{q}}$ is the heat-flux vector; $\breve{\boldsymbol{D}}$ is the rate-of-deformation tensor; $\boldsymbol{I}$ is the identity tensor; $\breve{\mu} = \mu(\tilde{T})$ is the molecular dynamic viscosity at temperature $\tilde{T}$; μ_T is the eddy viscosity; $\breve{\kappa} = \kappa(\tilde{T})$ is the molecular heat conductivity at temperature $\tilde{T}$; κ_T is the eddy heat conductivity; $Re_T^* = k^2\varepsilon^{*-1}\breve{\nu}^{-1}$ is the turbulence Reynolds number, $\tilde{}$ is Favre averaging (with fluctuations $''$); $\bar{}$ is nonweighted averaging (with fluctuations $'$); and $\breve{}$ are functions of mean flow quantities that cannot be identified with the preceding averages. The model constants, model functions, molecular-diffusion coefficients, and other details are given in Refs. 33 and 34. The tensor-invariant form for the near-wall source term in the ε equation $2\breve{\nu}\mu_T[\nabla^2\tilde{\boldsymbol{W}}]^2$ used in the present work was introduced by Gerolymos.[38] It satisfies Galilean invariance requirements in the rotating frame of reference[39] while giving results equivalent to those obtained using the formulation suggested by Launder et al.[40]

Computational Grid and Navier–Stokes Solver

Let (x, R, θ) be a cylindrical coordinates system, with $\boldsymbol{e}_x$ the engine axis, and (x, y, z) an associated Cartesian coordinate system ($y = R\cos\theta$ and $z = R\sin\theta$), both rotating with the blade-row rotation rate, $\boldsymbol{\Omega} = \Omega\boldsymbol{e}_x$. The computational grid used is a structured H–O–H grid, generated automatically using the grid-generation methodology described by Tsanga[41] and Gerolymos and Tsanga[42] (Fig. 1). An embedded O-type grid (TC grid) is added within the tip-clearance gap. This grid is stretched both near the casing and at the blade tip (Fig. 2). The tip-clearance flow that leaves the blade tip forms a jet-like structure that interacts with the interblade flowfield. To capture this structure correctly, a patched O-type zoom grid (OZ grid) was introduced. This grid spans radially from the casing to a given radial depth δ_{OZ} beneath it. The $i_{\mathrm{OZ}} =$ const planes and the $j_{\mathrm{OZ}} =$ const planes of the OZ grid coincide with the $i_{\mathrm{O}} =$ const and the $j_{\mathrm{O}} =$ const planes of the O grid. In the radial direction the OZ-grid points coincide with the TC-grid points at the TC–OZ boundary. The OZ-grid points are stretched beneath the blade tip until an O-grid radial plane $k_{\mathrm{O}} = k_{\mathrm{O-OZ}}$ where the OZ-grid points coincide with the O-grid points. This patched zoom-grid technique allows the refinement of the tip-clearance flow grid, independently of the external blade O grid. Further details on the grid-generation technique are given by Gerolymos and Tsanga.[42]

The mean-flow and turbulence-transport equations are written in the (x, y, z) Cartesian rotating (relative) coordinates system and

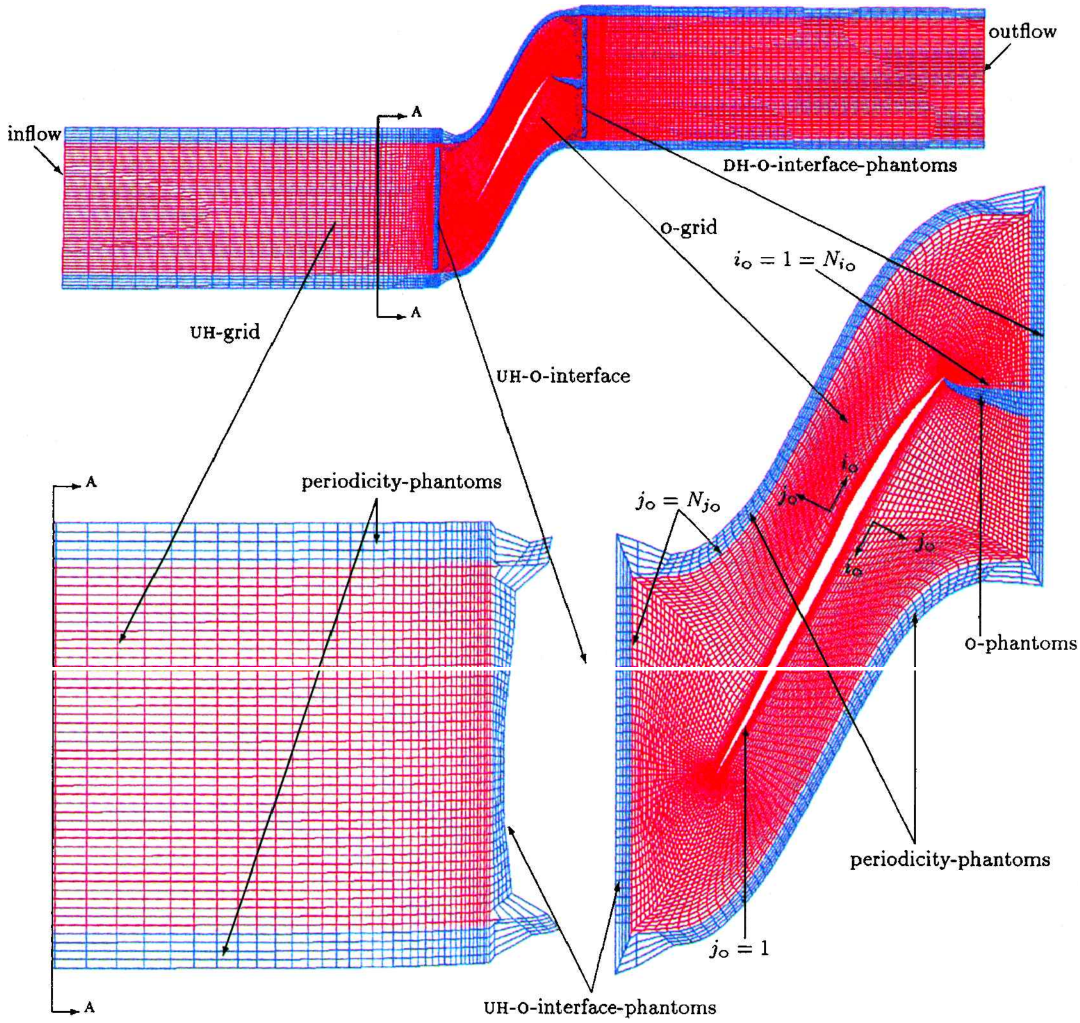

Fig. 1 Phantom nodes used for H–O interfaces and periodicity conditions: red line, computational grid, and blue line, phantom nodes.

are discretized in space on a structured grid, using a third-order, upwind-biased MUSCL scheme with Van Leer flux-vector splitting and Van Albada limiters, and the resulting semidiscrete scheme is integrated in time using a first-order implicit procedure.[34] The mean-flow and turbulence-transport equations are integrated simultaneously. The Jacobian-flux matrix is computed using a first-order space discretization for the convective fluxes, to reduce bandwidth. The Jacobian matrix for the viscous terms is approximated by a spectral-radius matrix. The Jacobian matrix is factored, and the resulting linear systems are solved by lower–upper decomposition. The numerical method is described in detail by Vallet[33] and Gerolymos and Vallet.[34] Source terms (centrifugal, Coriolis, and k–ε) are treated explicitly (preliminary numerical tests showed that their implicit treatment does not influence the numerical stability of the method), and the $\frac{1}{2}\Omega^2 R^2 \bar{\rho} \tilde{\boldsymbol{W}}$ term in the rothalpy fluxes is mass split as $\mathfrak{f}_m^{\pm} \frac{1}{2}\Omega^2 R^2$, where $\mathfrak{f}_m^{\pm}$ is the mass flux.[41]

The local time step is based on a combined convective (Courant) and viscous (von Neumann) criterion.[33,34] The convective time step is computed using the relative flow velocity $\tilde{W}$. For steady turbomachinery computations, CFL $= 20$ is used with local time stepping. The approximate factorization along grid lines used in the alternating-direction, implicit time integration introduces a truncation error that limits CFL, as shown by Lin et al.,[43] especially in regions where the flow is completely misaligned with grid directions, such as leading edges, trailing edges, and H–O interface corners (Fig. 2). To ensure stability in all of the cases studied, the CFL was linearly reduced from 20 to 5, within a radius of $\frac{1}{4}\chi(k)$ (where χ is the blade chord at a given k section) around the leading edge, the trailing edge, and the O-grid corners. The same procedure is applied at the blade-tip edge, within a radius of $\frac{1}{2}\delta_{\mathrm{TC}}$.

To ensure the stability of the method, it is necessary to introduce limiters for k and ε, which may otherwise diverge toward nonphysical values. The very simple and particularly efficient limiters introduced by Vallet[33] and Gerolymos and Vallet[34,35] were used (with a maximum admissible length scale $\ell_{T_{\max}}$ typically one-half the meridional channel height). These simple positivity and boundedness fixes stabilize the computations in all of the cases studied.

The flowfield is initialized by linearly interpolating pressure between inflow and outflow and assuming isentropic adiabatic evolution. Near the solid boundaries, analytic flat-plate profiles are fitted. The mean flow and turbulence profiles are obtained analytically in a manner similar to that of Gerolymos.[38] The details for the initialization procedure are given by Vallet[33] and Tsanga.[41]

The numerical scheme is not applied at the singular points of the TC grid,[42] where the flow variables are obtained, at every iteration, by interpolation from the neighboring nodes.

Boundary Conditions

To use high-CFL time steps, boundary conditions are applied both explicitly and implicitly,[33,44] and a phantom-node technique is applied at grid interfaces.

At solid walls (hub, casing, blades), a standard adiabatic no-slip wall condition is applied:

$$\tilde{\boldsymbol{V}} = \boldsymbol{V}_w, \qquad \frac{\partial \bar{p}}{\partial n} \cong 0, \qquad \frac{\partial \tilde{T}}{\partial n} \cong 0 \tag{3}$$

where n is the direction normal to the wall and $\boldsymbol{V}_w$ is the velocity of the solid wall ($\boldsymbol{V}_w = 0$ on fixed surfaces, and $\boldsymbol{V}_w = \Omega R \boldsymbol{e}_\theta$ on rotating surfaces, such as rotor blades and rotating parts of the hub).

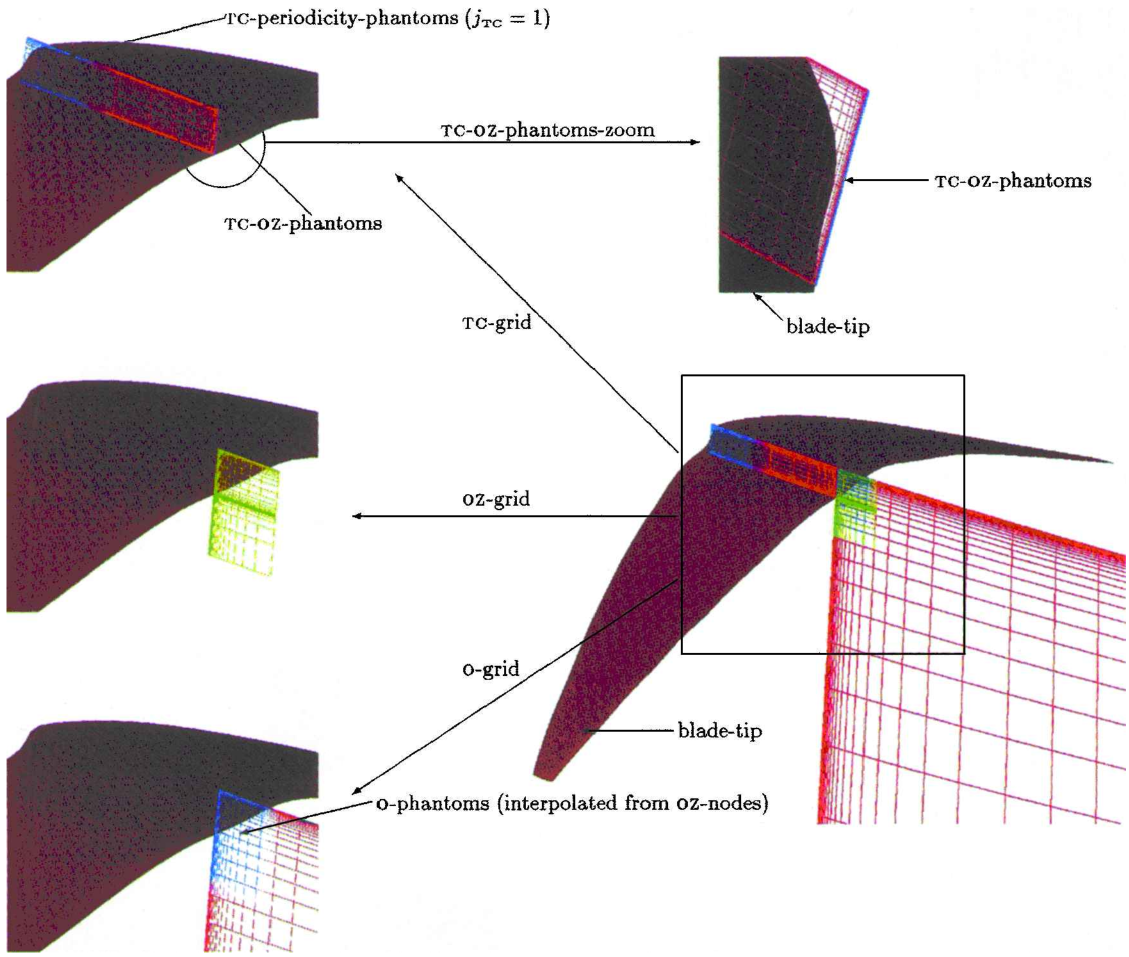

Fig. 2 Phantom nodes used for tip-clearance interfaces: red line, computational grid; blue line, phantom nodes; and green line, patched nodes.

Periodicity conditions and conditions at H–O interfaces are applied using a phantom-node technique (Fig. 1). This is necessary because an implicit periodicity boundary condition would increase matrix bandwidth, requiring greater computer memory, whereas implicit matching between domains is even more complex. The computational grid is extended i-wise and j-wise for both the H grids and the O grid, using five phantom nodes. To avoid interpolations for phantom-node updating, these nodes correspond to grid nodes of the neighboring domain, exploiting grid topology and periodicity. The phantom nodes for periodicity are obtained by a $\pm 2\pi/N_B$ rotation of existing grid points, where N_B is the number of blades. At H–O interfaces, phantom nodes of the H grid are constructed using O-grid nodes, and vice versa. The O-grid points at $i_O = 1$ and N_{i_O} coincide $\forall j, k$, and the grid is extended, exploiting the O periodicity. The periodicity and H–O-interface phantom nodes are updated at the end of each iteration from the corresponding grid nodes. Implicit no-change boundary conditions ($\partial \boldsymbol{w}/\partial t = 0$) are applied at the edge phantom nodes both i-wise ($i_{UH} = N_{i_{UH}} + 5$, $i_{DH} = -4$, $i_O = -4$; $N_{i_O} + 5, \forall j, k$) and j-wise ($j_{UH} = -4$; $N_{j_{UH}} + 5$, $j_{DH} = -4$; $N_{j_{DH}} + 5$, $j_O = N_{j_O} + 5$).

A reservoir condition is applied at inflow, assumed to be an axial plane $\perp \boldsymbol{e}_x$ ($x = x_{in}$):

$$x = x_{in} : \left[\frac{\partial \breve{p}_t}{\partial t} = 0,\ \frac{\partial \breve{h}_t}{\partial t} = 0,\ \frac{\partial \breve{\alpha}}{\partial t} = 0,\ \frac{\partial \breve{\phi}}{\partial t} = 0\right] \quad \forall R, \theta \tag{4}$$

where $\breve{p}_t$ is the total pressure at inflow, $\breve{h}_t$ is the total enthalpy at inflow, $\breve{\alpha} = \angle(\tilde{\boldsymbol{V}}, \boldsymbol{e}_\theta)$, and $\breve{\phi} = \angle(\tilde{\boldsymbol{V}}_m, \boldsymbol{e}_R)$ (with $\tilde{\boldsymbol{V}}_m = \tilde{V}_x \boldsymbol{e}_x + \tilde{V}_R \boldsymbol{e}_R$).

At the outflow boundary, assumed to be an axial plane $\perp \boldsymbol{e}_x$ ($x = x_{out}$), the ratio of the pressure at the casing $\bar{p}_{casing}$ to the mass flow $\dot{m}_{out}$, $\pi_{\dot{m}}$ is imposed, together with a radial-equilibrium condition

$$x = x_{out} : \left[\bar{p} = {}^{SCH}\dot{m}_{out}\,\pi_{\dot{m}},\quad R = R_{casing}, \forall \theta;\ \frac{\partial \bar{p}}{\partial R} = \frac{\rho_M V_{\theta_M}^2}{R}, \forall R, \theta\right] \tag{5}$$

where ${}^{SCH}\dot{m}_{out}$ is the mass flow computed by extrapolation before the application of the boundary conditions. All other variables are extrapolated from the interior. This condition, suggested by Escuret in a private communication, is a back-pressure condition, reevaluated at every iteration. This condition is necessary in the case of unstarted flows[45] where, because of the great sensitivity of mass flow on small back-pressure variations, computations with a fixed back-pressure condition present a very slow but continuous divergence toward lower mass flows as the iteration counter increases.[41,46]

Periodicity conditions for the TC grid (at $j_{TC} = 1$ and at $i_{TC} = 1$; $N_{i_{TC}}$) are applied using five phantom nodes corresponding to actual nodes in the TC grid (Fig. 2). The information from the OZ grid is obtained using five phantom nodes (TC–OZ phantoms) corresponding to actual nodes in the OZ grid (Fig. 2).

The O-grid nodes that overlap with the OZ grid are updated at every iteration by line interpolation of OZ-grid nodes. The OZ-grid boundary conditions are 1) solid-wall conditions at the casing and on the blade surface and 2) matching (using simple averaging) with the TC-grid and O-grid values at the corresponding interfaces. (In the implicit phase the previously computed increments of the TC-grid and the O-grid nodes at the interfaces are applied as implicit boundary conditions for the OZ grid.)

Comparison with Measurements

Computational results are compared with measurements for the NASA 37 transonic rotor.[47,48] Experimental data for the NASA 37 transonic rotor were obtained at various measurement planes, using both laser Doppler velocimetry and classical rake measurements of p_{t_M} and T_{t_M}. (The averaging procedure indicated by subscript M is described in Ref. 47.) This rotor has 36 blades, nominal speed 17,188.7 rpm, and maximum mass flow at nominal speed $\dot{m}_{\text{CH}} = 20.93 \pm 0.14$ kg s^{-1}. The nominal tip-clearance gap is 0.356 mm (Ref. 48).

Computations of this configuration, including an embedded tip-clearance grid, have been presented by Chima,[32] using a Baldwin–Lomax mixing-length model and 13 radial stations within the tip-clearance gap, and by Hah and Loellbach,[18] using the k–ε closure of Chien[13] and 10 radial stations within the tip-clearance gap. In both cases the total number of grid points was $\sim 10^6$. Results for the nominal (near-peak-efficiency; $\dot{m} = 0.98$, $\dot{m}_{\text{CH}} = 20.51$ kg s^{-1}) operating point using the present method are presented by Gerolymos and Vallet.[49] Here the method is validated by comparison with measurements at a near-surge operating point ($\dot{m} = 0.92\dot{m}_{\text{CH}} = 19.36$ kg s^{-1}).

Computations were run on three grids (Table 1), grid B with 10^6 points, grid C with 2×10^6 points, and grid D with 3×10^6 points. There are two parameters determining grid quality in the boundary-layers: 1) the size of the first cell n_w^+ and 2) the stretching ratio r. Studies on shock-wave/boundary-layer interaction[33–35] have indicated that $n_w^+ \sim \frac{3}{4}$ is adequate in giving satisfactory results provided, however, that the geometric progression ratio is less than $\frac{3}{2}$. With this criterion (Table 1; Fig. 3), grid B is too coarse on the flow-path walls and on the blade tip, whereas grid C is an adequate grid. A finer and less stretched grid D (Table 1; Fig. 3) was also used to demonstrate grid convergence of the results.

Computational and experimental boundary conditions at inflow were $p_{t_{\text{in}}} = 101{,}325$ Pa, $T_{t_{\text{in}}} = 288.15$ K, $\alpha_{\text{in}} = 0$, $\phi_{\text{in}} = 0$, $T_{u_{\text{in}}} = 3\%$, where $p_{t_{\text{in}}}$, $T_{t_{\text{in}}}$, α_{in}, ϕ_{in}, and $T_{u_{\text{in}}}$ are the total pressure, total temperature, flow angles, and turbulence intensity $[T_u = \tilde{V}^{-1}\sqrt{(\frac{2}{3}k)}]$ outside the boundary layers at inflow. The inflow distributions included flat-plate boundary-layer profiles, fitted at the hub and the casing,[33,38,41] with thicknesses $\delta_{\text{hub}_{\text{in}}} = \delta_{\text{casing}_{\text{in}}} = 0.005$ m, based on measured total pressure profiles.

Convergence histories (Fig. 4) of mass flow, total-to-total pressure ratio $\pi_{\text{T-T}_\text{O}}$, and entropy rise Δs_O (between inflow and outflow of the O grid) using the finest grid D show that the computations converge at $\sim$700 iterations for the near-peak efficiency ($\dot{m} = 0.98\dot{m}_{\text{CH}}$) point, whereas they require twice as many iterations for the near-surge ($\dot{m} = 0.92\dot{m}_{\text{CH}}$) point. This is to be expected because near surge the flow is unstarted at the tip and very sensitive to small changes of outflow pressure.[41] This result is in contradiction with the work of Chima,[32] where the same number of iterations was used for both operating points. Note that the pressure ratio $\pi_{\text{T-T}_\text{O}}$ used to monitor convergence (Fig. 4) is measured at the outflow of the O grid located near station 3 (Fig. 5) and is, therefore, higher than the pressure ratio $\pi_{\text{T-T}}$ at station 4 (Table 1). The three grids overestimate the pressure ratio when compared to measurements and slightly underestimate efficiency (Table 1). The slight difference in mass flow between computations and measurements is within the experimental uncertainty of ± 0.14 kg s^{-1}.

Comparison of computed and measured radial distributions of appropriately pitchwise-averaged[47] total pressure p_{t_M} (nondimensionalized by $p_{t_{\text{ISA}}} = 101{,}325$ Pa), total temperature T_{t_M} (nondimensionalized by $T_{t_{\text{ISA}}} = 288.15$ K), flow angle $\alpha_{x\theta_M}$ (Ref. 48), and isentropic

Table 1 Computational grid summary

Grid	Points	N_{k_O}[a]	r_{k_O}[b]	$N_{k_{\text{TC}}}$[c]	$r_{k_{\text{TC}}}$[d]	δ_{OZ}[e]	$n_{w\text{B}}^+$[f]	$n_{w\text{FP}}^+$[g]	$\dot{m}$, kg s^{-1}	$\pi_{\text{T-T}}$[h]	η_{is}[i]
B	1,149,421	65	1.46	21	1.50	0.70	<0.3	<1.5	19.45	2.193	0.8379
C	1,955,587	101	1.26	31	1.45	0.70	<0.3	<1.0	19.46	2.175	0.8372
D	3,067,042	161	1.17	41	1.30	0.60	<0.3	<0.5	19.47	2.180	0.8401
Experiment	——	——	——	——	——	——	——	——	19.39	2.138	0.8496

[a]Number of radial stations (blade O-type grid). [b]k-wise geometric progression ratio (blade O-type grid).
[c]Number of radial stations (tip-clearance O-type grid). [d]k-wise geometric progression ratio (tip-clearance O-type grid).
[e]Radial extent of O-type zoom grid from the casing (millimeters). [f]Equal to n_w^+ on the blades.
[g]Equal to n_w^+ on the flow-path walls (hub and casing). [h]Between stations 1 and 4 (Fig. 5).
[i]Isentropic efficiency between stations 1 and 4 (Fig. 5).

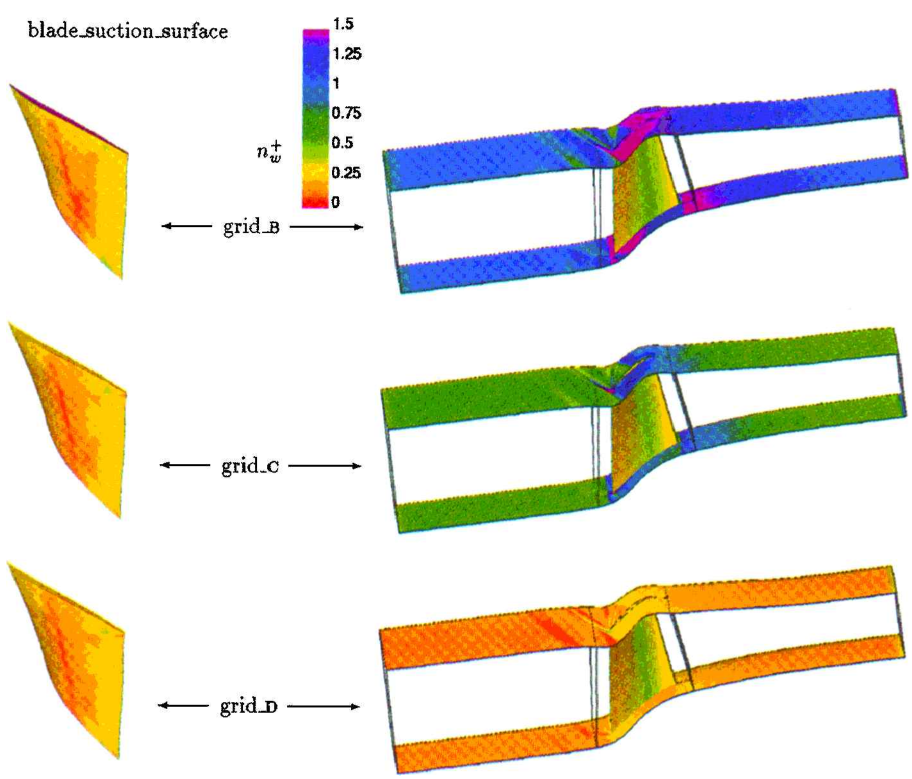

Fig. 3 Iso-n_w^+ contours for NASA 37 rotor ($\dot{m}$ = 0.92$\dot{m}_{\text{CH}}$, T_u = 3%, δ_{TC} = 0.356 mm).

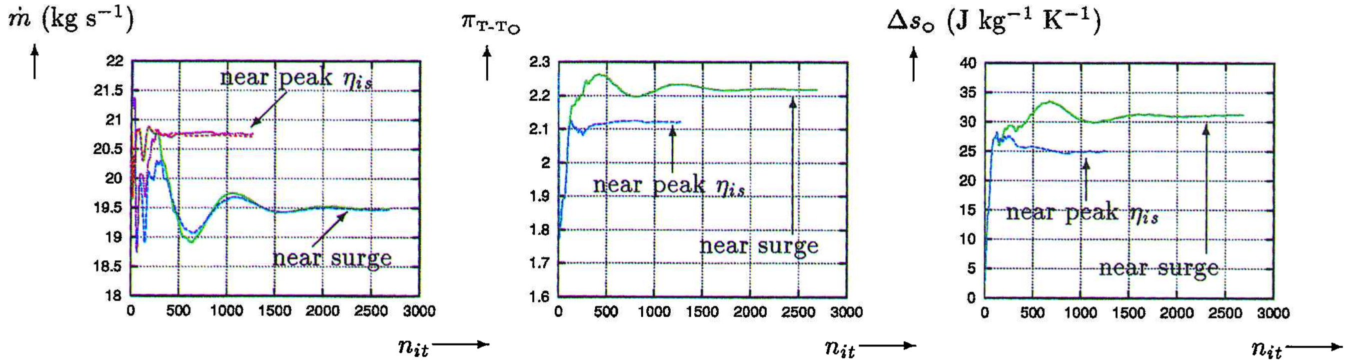

Fig. 4 Convergence of computations for NASA 37 rotor ($\dot{m} = 0.92\dot{m}_{\text{CH}}$, $0.98\dot{m}_{\text{CH}}$, $T_u = 3\%$, $\delta_{\text{TC}} = 0.356$ mm; grid D).

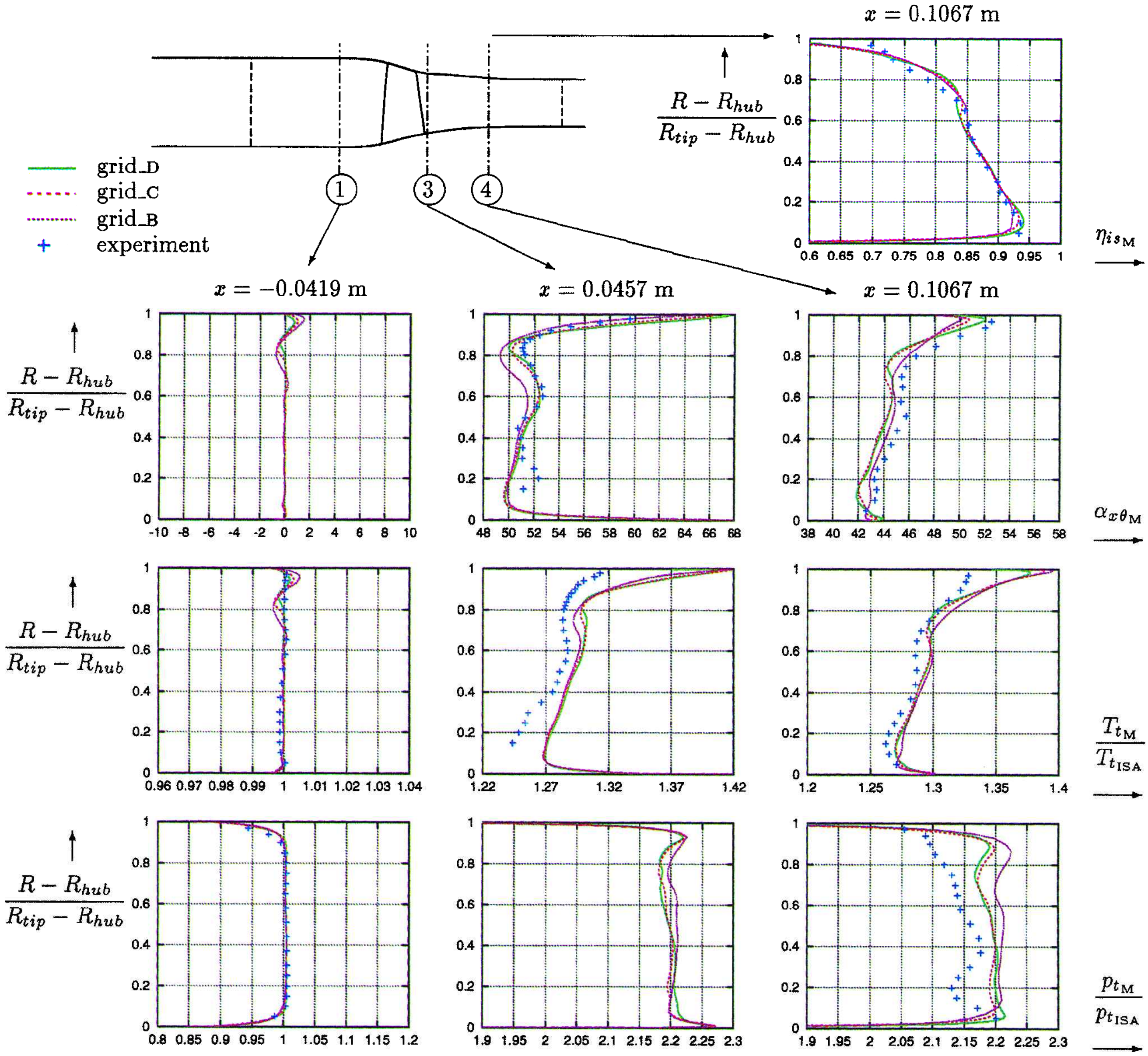

Fig. 5 Computed and measured radial distributions of pitchwise-averaged flow angle $\alpha_{x\theta_M}$, total pressure p_{t_M}, and total temperature T_{t_M}, for NASA 37 rotor ($\dot{m} = 0.92\dot{m}_{\text{CH}}$, $T_u = 3\%$, $\delta_{\text{TC}} = 0.356$ mm).

efficiency η_{is_M} at station 4 (Fig. 5) shows good overall agreement. Results using grids C and D are practically identical everywhere, demonstrating grid convergence of results. Results using the coarsest grid B are slightly different. At station 1, comparison of p_{t_M} plots shows that the boundary-layer thickness used for the inflow boundary conditions is correct. At rotor exit (station 3) the flow angle $\alpha_{x\theta_M}$ is very well predicted, with the exception of an overturning peak at 20% span, associated with rotor hub secondary flows that are not predicted by the method. The T_{t_M} distribution is slightly overestimated at station 3, but this discrepancy is not visible at station 4 (Fig. 5), with the exception of the systematic prediction of higher temperatures near the casing. Flow angles are correct to within 1 deg, with the finest grid D being more accurate near the casing. The p_{t_M} distribution at station 4 shows an overestimation of pressure ratio, as is the case with all other published results.[18,32] The overshoot of p_{t_M} near the casing appears in most computations using k–ε models

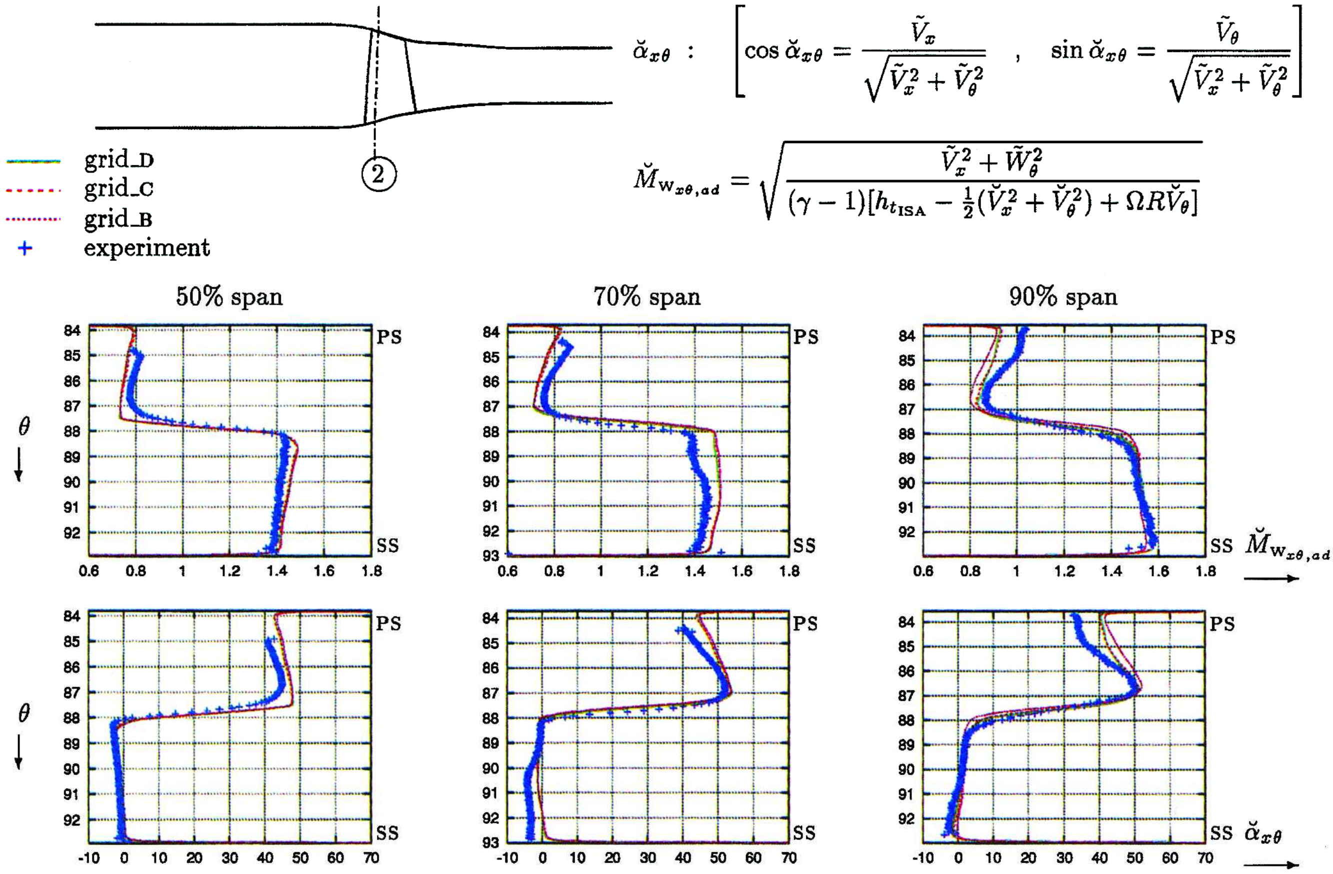

Fig. 6 Comparison of computed and measured pitchwise distributions of $\breve{M}_{W_{x\theta,ad}}$ and $\breve{\alpha}_{x\theta}$ for NASA 37 rotor ($\dot{m}$ = 0.92$\dot{m}_{CH}$, T_u = 3%, δ_{TC} = 0.356 mm).

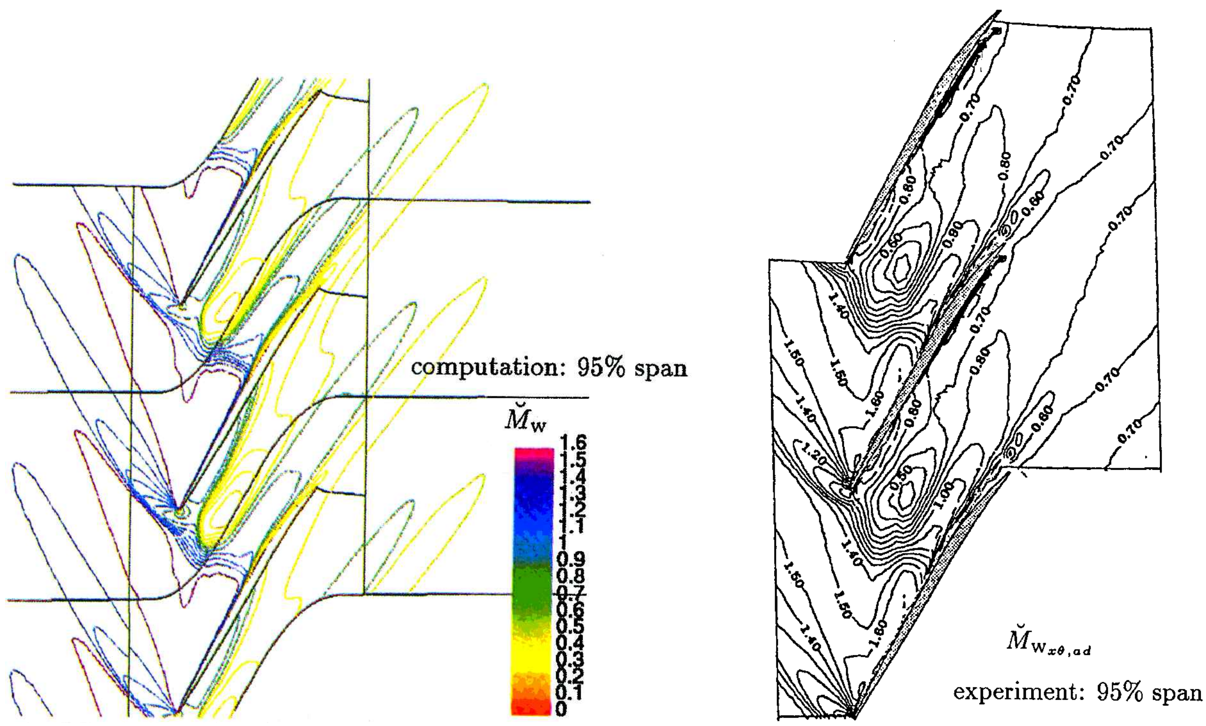

Fig. 7 Computed and measured iso-$\breve{M}_W$ contours for NASA 37 rotor ($\dot{m}$ = 0.92$\dot{m}_{CH}$, T_u = 3%, δ_{TC} = 0.356 mm; grid D).

(either near wall[18] or with wall functions[50]) and is presumably due to a deficiency of the model to correctly predict the complex three-dimensional mixing of the near-casing flow. In the near-hub region, the deficit in total pressure is underpredicted. Hah and Loellbach[18] attribute this effect to important corner stall, whereas Shabbir et al.[50] attribute the deficit in total pressure near the hub to possible leakage flow emanating from the small gap between the stationary and rotating parts of the hub flow path upstream of the rotor. Based on the well-established underprediction of flow separation by the k–ε closure used,[33–35,38] the present authors believe that part of this discrepancy is due to turbulence modeling. The η_{is_M} distribution is well predicted (Fig. 5).

Comparison of relative Mach number $\breve{M}_{W_{x\theta,ad}}$ and flow angle $\breve{\alpha}_{x\theta}$ (computed using only the x and θ velocity components and assuming rothalpy conservation as was done for the experiment[48]) at 20% axial chord and at different spanwise stations gives good

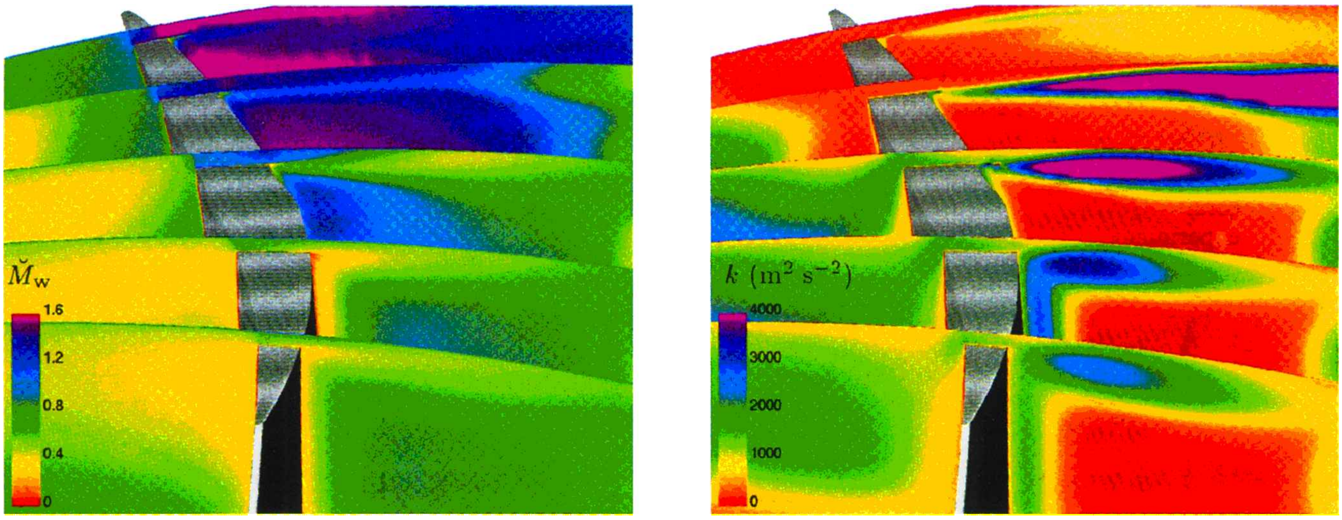

Fig. 8 Plots of $\breve{M}_W$ and k near the blade tip of NASA 37 rotor ($\dot{m}$ = 0.92$\dot{m}_{\mathrm{CH}}$, T_u = 3%, δ_{TC} = 0.356 mm; grid D).

agreement (Fig. 6). The results using the three grids are practically identical. The predicted and measured flow structure at 95% span (Fig. 7) are in good agreement concerning shock structure, shock strength, and leakage-flow structure.

The same conclusions hold at the near-peak-efficiency operating point.[49]

The detail of the flow over the blade tip (Fig. 8) clearly shows the flow acceleration from the pressure side, over the blade tip, and the jet-like structure of the flow discharged toward the suction side. There are very important levels of k within the tip-clearance gap (Fig. 8), suggesting that turbulence modeling inside the gap is important. This is in agreement with Chima,[32] who reports the sensitivity of results on the implementation of the Baldwin–Lomax mixing-length turbulence model used inside the gap.

Conclusions

A three-dimensional compressible Navier–Stokes solver, using near-wall, low-turbulence Reynolds number k–ε closure is described and applied to the computation of axial turbomachinery flow. The method uses a multiblock-grid approach to accurately compute the details of tip-clearance flow. Exchange of information between the tip-clearance O grid and the blade O grid is transmitted using a patched grid technique that offers high grid resolution, locally at the blade tip. The resulting method is particularly robust.

An initial validation against experimental data shows satisfactory agreement. Grid refinement studies demonstrate the need of quite fine grids for the accurate computation of transonic compressor flows. Grid refinement is necessary both in the immediate vicinity of solid walls and in the secondary flow region. Refinement of the tip-clearance grid influences the total temperature distribution near the casing. For accurate results, as far as grid refinement is concerned, two conditions must be met: 1) the nondimensional grid-cell size at the wall $n_w^+ < \frac{3}{4}$ and 2) the stretching ratio $r < \frac{3}{2}$. Comparison between different grids and with measurements shows that grid-converged results can be obtained with 2×10^6–3×10^6 points for transonic compressor rotors (results with 10^6 points give quite similar but not identical results).

Improvement of turbulence closure is necessary for enhancing the accuracy of flow prediction. The major drawbacks of the k–ε closure used appear in the underestimation of hub corner separation and also in the secondary flow mixing near the casing.

Acknowledgments

The support of the Région Ile-de-France through a SESAME Grant is acknowledged. The computations presented were run at the Institut pour le Développement des Ressources en Informatique Scientifique, where computer resources were made available by the Comité Scientifique. This work is part of the turbo-3D project of the Laboratoire d'Energétique, Université Pierre-et-Marie-Curie. The authors are listed alphabetically. The authors are grateful to J. F. Escuret, SNECMA, Villaroche, France, for his 1996 private communication.

References

[1]Lakshminarayana, B., "Turbulence Modeling for Complex Shear Flows," *AIAA Journal*, Vol. 24, No. 12, 1986, pp. 1900–1917.

[2]Leschziner, M. A., "Computation of Aerodynamic Flows with Turbulence-Transport Models Based on 2-Moment Closure," *Computers and Fluids*, Vol. 24, No. 4, 1995, pp. 377–392.

[3]Dawes, W. N., "The Simulation of 3-D Viscous Flow in Turbomachinery Geometries Using a Solution-Adaptive Unstructured Mesh Methodology," *Journal of Turbomachinery*, Vol. 114, No. 3, 1992, pp. 528–537.

[4]Turner, M. G., and Jennions, I. K., "An Investigation of Turbulence Modeling in Transonic Fans Including a Novel Implementation of an Implicit k–ε Turbulence Model," *Journal of Turbomachinery*, Vol. 115, No. 2, 1993, pp. 249–260.

[5]Kwon, O. J., and Hah, C., "Simulation of Three-Dimensional Turbulent Flows on Unstructured Meshes," *AIAA Journal*, Vol. 33, No. 6, 1995, pp. 1081–1089.

[6]Hah, C., "A Numerical Modeling of Endwall and Tip-Clearance Flow of an Isolated Compressor Rotor," *Journal of Engineering for Gas Turbines and Power*, Vol. 108, No. 1, 1986, pp. 15–21.

[7]Hah, C., Bryans, A. C., Moussa, Z., and Tomsho, M. E., "Application of Viscous Flow Computations for the Aerodynamic Performance of a Backswept Impeller at Various Operating Conditions," *Journal of Turbomachinery*, Vol. 110, No. 3, 1988, pp. 303–311.

[8]Knight, C. J., and Choi, D., "Development of a Viscous Cascade Code Based on Scalar Implicit Factorization," *AIAA Journal*, Vol. 27, No. 5, 1989, pp. 581–594.

[9]Kunz, R. F., and Lakshminarayana, B., "3-D Navier–Stokes Computation of Turbomachinery Flows Using an Explicit Numerical Procedure and a Coupled k–ε Turbulence Model," *Journal of Turbomachinery*, Vol. 114, No. 3, 1992, pp. 627–642.

[10]Ameri, A. A., Steinthorsson, E., and Rigby, D. L., "Effect of Squealer Tip on Rotor Heat Tranfer and Efficiency," *Journal of Turbomachinery* (to be published); also American Society of Mechanical Engineers Paper 97-GT-128, 1997.

[11]Ameri, A. A., and Steinthorsson, E., "Prediction of Unshrouded Rotor Blade Tip Heat Transfer," American Society of Mechanical Engineers Paper 95-GT-142, 1995.

[12]Ameri, A. A., and Steinthorsson, E., "Analysis of Gas Turbine Rotor Blade Tip and Shroud Heat Transfer," American Society of Mechanical Engineers Paper 96-GT-189, 1996.

[13]Chien, K. Y., "Predictions of Channel and Boundary-Layer Flows with a Low-Reynolds Number Turbulence Model," *AIAA Journal*, Vol. 20, No. 1, 1982, pp. 33–38.

[14]Hah, C., "Calculation of Three-Dimensional Viscous Flows in Turbomachinery with an Implicit Relaxation Method," *Journal of Propulsion and Power*, Vol. 3, No. 5, 1987, pp. 415–422.

[15]Copenhaver, W. W., Mayhew, E. R., Hah, C., and Wadia, A. R., "The Effect of Tip Clearance on a Swept Transonic Compressor Rotor," *Journal of Turbomachinery*, Vol. 118, No. 2, 1996, pp. 230–239.

[16]Copenhaver, W. W., Puterbaugh, S. L., and Hah, C., "Unsteady Flow and Shock Motion in a Transonic Compressor Rotor," *Journal of Propulsion and Power*, Vol. 13, No. 1, 1997, pp. 17–23.

[17]Hah, C., Puterbaugh, S. L., and Copenhaver, W. W., "Unsteady Aerodynamic Flow Phenomena in a Transonic Compressor Stage," *Journal of Propulsion and Power*, Vol. 13, No. 3, 1997, pp. 329–333.

[18]Hah, C., and Loellbach, J., "Development of Hub Corner Stall and Its Influence on the Performance of Axial Compressor Blade Rows," *Journal of Turbomachinery* (to be published); also American Society of Mechanical Engineers Paper 97-GT-42, 1997.

[19]Coakley, T. J., "Turbulence Modeling Methods for the Compressible Navier–Stokes Equations," AIAA Paper 83-1693, 1983.

[20]Coakley, T. J., "Implicit Upwind Methods for the Compressible Navier–Stokes Equations," *AIAA Journal*, Vol. 23, No. 3, 1985, pp. 374–380; also NASA TM-85899, Feb. 1984.

[21]Kunz, R. F., and Lakshminarayana, B., "Stability of Explicit Navier–Stokes Procedures Using k–ε and k–ε/Algebraic Reynolds Stress Turbulence Models," *Journal of Computational Physics*, Vol. 103, 1992, pp. 141–159.

[22]Kunz, R. F., Lakshminarayana, B., and Basson, A. H., "Investigation of Tip-Clearance Phenomena in an Axial Compressor Cascade Using Euler and Navier–Stokes Procedures," *Journal of Turbomachinery*, Vol. 115, No. 3, 1993, pp. 453–467.

[23]Wilcox, D. C., "Simulation of Transition with a Two-Equation Turbulence Model," *AIAA Journal*, Vol. 32, No. 2, 1994, pp. 247–255.

[24]Denton, J. D., "Loss Mechanisms in Turbomachines," *Journal of Turbomachinery*, Vol. 115, No. 4, 1993, pp. 621–656.

[25]Storer, J. A., and Cumpsty, N. A., "An Approximate Analysis and Prediction Method for Tip Clearance Loss in Axial Compressors," *Journal of Turbomachinery*, Vol. 116, No. 4, 1994, pp. 648–656.

[26]Lakshminarayana, B., *Fluid Dynamics and Heat Transfer of Turbomachinery*, Wiley, New York, 1997.

[27]Basson, A. H., Kunz, R. F., and Lakshminarayana, B., "Grid Generation for 3-D Turbomachinery Geometries Including Tip Clearance," *Journal of Propulsion and Power*, Vol. 9, No. 1, 1993, pp. 59–66.

[28]Rai, M. M., "Three-Dimensional Navier–Stokes Simulations of Turbine Rotor-Stator Interaction: Part I. Methodology," *Journal of Propulsion and Power*, Vol. 5, No. 3, 1989, pp. 305–311.

[29]Rai, M. M., "Three-Dimensional Navier–Stokes Simulations of Turbine Rotor-Stator Interaction: Part II. Results," *Journal of Propulsion and Power*, Vol. 5, No. 3, 1989, pp. 312–319.

[30]Liu, J. S., and Bozzola, R., "Three-Dimensional Navier–Stokes Analysis of Tip Clearance Flow in Linear Turbine Cascades," *AIAA Journal*, Vol. 31, No. 11, 1993, pp. 2068–2074.

[31]Basson, A., and Lakshminarayana, B., "Numerical Simulation of Tip Clearance Effects in Turbomachinery," *Journal of Turbomachinery*, Vol. 117, No. 3, 1995, pp. 348–359.

[32]Chima, R. V., "Calculation of Tip Clearance Effects in a Transonic Compressor Rotor," *Journal of Turbomachinery*, Vol. 120, No. 1, 1998, pp. 131–140.

[33]Vallet, I., "Aérodynamique Numérique 3-D Instationnaire avec Fermeture Bas-Reynolds au Second Ordre," Ph.D. Thesis, Univ. Pierre-et-Marie-Curie, Paris, Dec. 1995.

[34]Gerolymos, G. A., and Vallet, I., "Implicit Computation of the Three-Dimensional Compressible Navier–Stokes Equations Using k–ε Turbulence Closure," *AIAA Journal*, Vol. 34, No. 7, 1996, pp. 1321–1330.

[35]Gerolymos, G. A., and Vallet, I., "Near-Wall Reynolds Stress Three-Dimensional Transonic Flows Computation," *AIAA Journal*, Vol. 35, No. 2, 1997, pp. 228–236.

[36]Rizzi, A., Eliasson, P., Lindblad, I., Hirsch, C., Lacor, C., and Haeuser, J., "The Engineering of Multiblock/Multigrid Software for Navier–Stokes Flows on Structured Meshes," *Computers and Fluids*, Vol. 22, No. 2/3, 1993, pp. 341–367.

[37]Launder, B. E., and Sharma, B. I., "Application of the Energy Dissipation Model of Turbulence to the Calculation of Flows Near a Spinning Disc," *Letters in Heat and Mass Transfer*, Vol. 1, 1974, pp. 131–138.

[38]Gerolymos, G. A., "Implicit Multiple-Grid Solution of the Compressible Navier–Stokes Equations Using k–ε Turbulence Closure," *AIAA Journal*, Vol. 28, No. 10, 1990, pp. 1707–1717.

[39]Speziale, C. G., "Turbulence Modeling in Noninertial Frames of Reference," *Theoretical and Computational Fluid Dynamics*, Vol. 1, 1989, pp. 3–19.

[40]Launder, B. E., Reynolds, W. C., Rodi, W., Mathieu, J., and Jeandel, D., *Turbulence Models and their Applications II*, Eyrolles, Paris, 1984.

[41]Tsanga, G., "Aérodynamique Numérique 3-D des Turbomachines Axiales Multiéetages avec Fermeture k–ε Bas-Reynolds," Ph.D. Thesis, Univ. Pierre-et-Marie-Curie, Paris, Jan. 1997.

[42]Gerolymos, G. A., and Tsanga, G., "Biharmonic Three-Dimensional Grid Generation for Axial Turbomachinery with Tip Clearance," *Journal of Propulsion and Power* (submitted for publication).

[43]Lin, H., Yang, D. Y., and Chieng, C. C., "Variants of Biconjugate–Gradient Method for Compressible Navier–Stokes Solver," *AIAA Journal*, Vol. 33, No. 7, 1995, pp. 1177–1184.

[44]Chakravarthy, S. R., "Euler Equations: Implicit Schemes and Boundary Conditions," *AIAA Journal*, Vol. 21, No. 5, 1983, pp. 699–706.

[45]Lichtfuss, H. J., and Starken, H., "Supersonic Cascade Flow," *Progress in Aerospace Sciences*, Vol. 15, 1974, pp. 37–149.

[46]Gerolymos, G. A., Blin, E., and Quiniou, H., "Comparison of Inviscid Computations with Theory and Experiment in Vibrating Transonic Compressor Cascades," *Recherche Aérospatiale*, Vol. 1991·6, 1991, pp. 63–82.

[47]Davis, R. L., Delaney, R. A., Denton, J. D., Giles, M. B., Strazisar, A. J., and Wisler, D. C., "CFD Code Assessment in Turbomachinery—Author's Information Package," American Society of Mechanical Engineers Turbomachinery Committee, 1993.

[48]Strazisar, A. J., "Data Report and Data Diskette for NASA Transonic Compressor Rotor 37," NASA Lewis Research Center, Cleveland, OH, 1994.

[49]Gerolymos, G. A., and Vallet, I., "Tip-Clearance and Secondary Flows in a Transonic Compressor Rotor," *Journal of Turbomachinery* (to be published); also American Society of Mechanical Engineers Paper 98-GT-366, 1998.

[50]Shabbir, A., Celestina, M. L., Adamczyk, J. J., and Strazisar, A. J., "The Effect of Hub Leakage on 2 High Speed Axial Flow Compressor Rotors," American Society of Mechanical Engineers Paper 97-GT-346, 1997.

F. W. Chambers
Associate Editor

Color reproduction courtesy of Université Pierre-et-Marie-Curie